Extracellular matrix stiffness causes systematic variations in proliferation and chemosensitivity in myeloid leukemias

Jae-Won Shin[a,b,c] and David J. Mooney[a,1]

[a]School of Engineering and Applied Sciences, Wyss Institute for Biologically Inspired Engineering, Harvard University, Cambridge, MA 02138; [b]Department of Pharmacology, University of Illinois College of Medicine, Chicago, IL 60612; and [c]Department of Bioengineering, University of Illinois College of Medicine, Chicago, IL 60612

Edited by Kristi S. Anseth, Howard Hughes Medical Institute, University of Colorado Boulder, Boulder, CO, and approved September 2, 2016 (received for review July 14, 2016)

Extracellular matrix stiffness influences biological functions of some tumors. However, it remains unclear how cancer subtypes with different oncogenic mutations respond to matrix stiffness. In addition, the relevance of matrix stiffness to in vivo tumor growth kinetics and drug efficacy remains elusive. Here, we designed 3D hydrogels with physical parameters relevant to hematopoietic tissues and adapted them to a quantitative high-throughput screening format to facilitate mechanistic investigations into the role of matrix stiffness on myeloid leukemias. Matrix stiffness regulates proliferation of some acute myeloid leukemia types, including *MLL-AF9*$^+$ MOLM-14 cells, in a biphasic manner by autocrine regulation, whereas it decreases that of chronic myeloid leukemia *BCR-ABL*$^+$ K-562 cells. Although Arg-Gly-Asp (RGD) integrin ligand and matrix softening confer resistance to a number of drugs, cells become sensitive to drugs against protein kinase B (PKB or AKT) and rapidly accelerated fibrosarcoma (RAF) proteins regardless of matrix stiffness when *MLL-AF9* and *BCR-ABL* are overexpressed in K-562 and MOLM-14 cells, respectively. By adapting the same hydrogels to a xenograft model of extramedullary leukemias, we confirm the pathological relevance of matrix stiffness in growth kinetics and drug sensitivity against standard chemotherapy in vivo. The results thus demonstrate the importance of incorporating 3D mechanical cues into screening for anticancer drugs.

matrix stiffness | systems pharmacology | biomaterials | drug screening | cancer

Myeloid leukemias originate from the hematopoietic stem cell compartment in bone marrow (BM) after oncogenic mutations. For instance, a translocation between parts of the human chromosome 22 and 9 results in the *BCR-ABL* fusion gene that causes chronic myeloid leukemia (CML) (1). Some translocations involving the mixed lineage leukemia (*MLL*) gene in the human chromosome 11, band q23, such as the *MLL-AF9* fusion gene, are involved in acute myeloid leukemia (AML) (2). In addition to mutations, hematopoietic microenvironments can contribute to pathogenesis and progression of myeloid leukemias (3). Both oncoproteins and cell-extrinsic factors are known to perturb various signaling pathways that regulate key biological processes in cancer. For instance, AKT/PKB (protein kinase B) is a major signaling node downstream of activated tyrosine kinases and phosphatidylinositol 3-kinase and has been targeted by a number of drugs to inhibit cancer cell survival and growth (4). Recently, physical cues from microenvironments have emerged as important regulators of tumor biology, such as extracellular matrix stiffness and collagen architecture (5, 6). Matrix stiffness also regulates normal hematopoiesis (7, 8). However, the relevance of physical cues to blood cancer remains largely unclear. Importantly, how different cancer subtypes with distinct oncogenic mutations respond to matrix stiffness also remains to be investigated.

Recent studies highlight the utility of adapting 3D culture into a high-throughput screening assay to better predict in vivo efficacy of anticancer drugs compared with conventional 2D culture (9, 10). However, physical properties of microenvironments were not considered in this assay format for cancer drug discovery. Effects of matrix stiffness on chemosensitivity were previously evaluated with breast cancer (11) and hepatocellular carcinoma cells (12) on 2D hydrogel systems, and with melanoma cells in 3D hydrogel systems (13). However, it is not clear whether these in vitro results inform in vivo drug efficacy. In general, it is largely unknown whether 3D matrix stiffness systematically influences responses of cancer cells to different drugs and potentially contributes to a failure to eradicate residual disease.

Here, we introduce a niche-based quantitative biophysical screen to evaluate the impact of 3D matrix stiffness on proliferation and drug sensitivity of different human myeloid leukemia subtypes. First, we altered mechanical properties of hydrogels so that they can closely mimic a range of physiological tissue stiffness relevant to the hematopoietic system. Leukemia cells were then encapsulated in the hydrogels and dispensed into a 96-multiwell assay format. Mechanistic studies using this system revealed distinct growth patterns and pharmacodynamics profiles of drugs against different leukemia subtypes as a function of matrix mechanics, highlighting relationships between genetic mutations and physical environments. Finally, the same hydrogel system was used in an in vivo xenograft model to validate the in vitro findings that matrix softening leads to resistance against standard chemotherapy.

Results

Matrix Mechanics Differentially Regulates Proliferation of Myeloid Leukemia Subtypes. When blood cells differentiate in the BM and traffic into the circulation, they transit from a solid-phase

Significance

Most chemotherapy drugs treat, but do not cure, cancer patients due to resistance. New high-throughput screening assays are emerging to better predict drug efficacy by recapitulating tumor microenvironments with three-dimensional hydrogels. Our platform exploits the mechanical tunability of alginate hydrogels to introduce biophysical cues into screening assays. The utility of this approach is demonstrated with the findings of unique modes of growth modulation by matrix stiffness and mechanosensitivity of drug actions in different myeloid leukemia subtypes. The same hydrogels were then adapted to confirm in vivo that matrix softening accelerates cancer growth kinetics and causes resistance to standard chemotherapy. We anticipate that this integrative workflow will be broadly useful to discover drugs that target cancer cells in different physical environments.

Author contributions: J.-W.S. and D.J.M. designed research; J.-W.S. performed research; J.-W.S. and D.J.M. analyzed data; and J.-W.S. and D.J.M. wrote the paper.

The authors declare no conflict of interest.

This article is a PNAS Direct Submission.

[1]To whom correspondence should be addressed. Email: mooneyd@seas.harvard.edu.

This article contains supporting information online at www.pnas.org/lookup/suppl/doi:10.1073/pnas.1611338113/-/DCSupplemental.

microenvironment to a viscous phase (14) (Fig. 1*A*). A similar transition also occurs outside the BM ("extramedullary" sites) when peripheral blood cells undergo intravasation from tissues. To generalize this mechanical transition, alginate was used to form hydrogels, because ionic cross-linking controls hydrogel stiffness independent of pore size, ensuring constant diffusion of molecules up to hundreds of kilodaltons (15). Importantly, adhesion ligands can be conjugated at different densities and controlled independent of stiffness. The hydrogel was conjugated with different densities of the Arg-Gly-Asp (RGD) peptide, which binds preferentially to $\alpha_5\beta_1$ and $\alpha_v\beta_3/\beta_5$ integrins, mixed with leukemia cells and ionically cross-linked to provide varied stiffness, ranging from soft solid (Young's modulus, E = 0.075~3 kPa) to viscous uncross-linked (E = "0" kPa) matrix in 96-well plates (Fig. S1*A*). Because the BM is generally viscoelastic (16), ionic cross-linking is more appropriate than covalent cross-linking because of the stress relaxation behavior (17). The average E for in situ BM is ~0.3 kPa (8). The minimum E achieved with alginate hydrogels is ~0.075 Pa (5), whereas ~3 kPa is close to the E of a number of soft tissues (18) or stiffer parts of the marrow. Without cross-linking, the alginate fluid in this study recapitulates the known viscosity value of blood under low shear (~40 cP) (16). This platform thus allows individualized ex vivo testing of disease progression and drug sensitivity in a high-throughput format, which could inform personalized therapies to target cancer cells in different biophysical environments (Fig. 1*A*).

We characterized how different myeloid leukemia subtypes with distinct genetic mutations respond to varied stiffness and ligand density. A representative human cell line from each myeloid leukemia subtype was used: AML with *MLL-AF9* (MOLM-14), AML without *MLL-AF9* (U-937), and CML with *BCR-ABL* (K-562). These cells are known to express $\alpha_5\beta_1$, which binds to the RGD sequence in fibronectin (19). In general, leukemia cells grow as amorphous aggregates in the viscous matrix and as single large spheres in the solid matrices (Fig. 1*A*). In all cases, there is a net increase in cell number of at least ~10-fold at day-7 culture. Within this time frame, AML cells show biphasic proliferation responses across matrix mechanics whereas CML cells show a stiffness-dependent decrease in cell number (Fig. 1*B*). Increasing RGD density significantly increases the maximal cell number at 0.3 kPa for MOLM-14, whereas it shifts the curve to the right for U-937. In contrast, ligand density does not significantly affect proliferation of K-562. Therefore, this screen is potentially useful to resolve each myeloid leukemia subtype based on distinct proliferation profiles as a function of matrix mechanics.

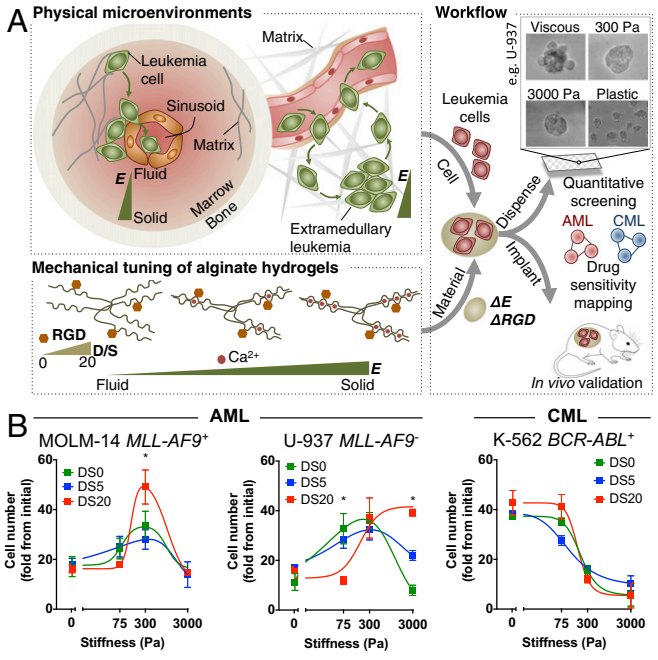

Fig. 1. Development of an integrative approach to systematically investigate the role of matrix mechanics in myeloid leukemias. (*A*) Schematic showing recapitulation of mechanical properties relevant to the hematopoietic system by ionic cross-linking of alginate hydrogels, followed by adaptation of the 3D hydrogels into quantitative screening and animal validation. (*B*) Different myeloid leukemia subtypes show distinct proliferative responses against matrix mechanics and ligand density. Ligand density is controlled by "degree of substitution" (DS), which indicates the number of RGD peptides conjugated per alginate molecule (0~20). The whole cell population was used for viability analysis. The data were fit to biphasic dose–response curves for AML cells and standard dose–response inhibition curves for CML cells. *$P < 0.05$ from one-way ANOVA with Tukey's honestly significant difference (HSD) test.

Autocrine Feedback Is Sufficient to Explain the Biphasic AML Growth with Matrix Stiffening. To explore mechanisms behind the biphasic response of AML cells, we asked whether matrix stiffening represents a component in biological circuits that can carry out two simultaneously opposing effects on cell growth and death. Because leukemia cells secrete a number of cytokines that can serve as autocrine signals (20), we hypothesized that matrix stiffening increases AML proliferation, but also leads to secretion of soluble factors that affect cell death. We first addressed this hypothesis by developing a computational model with a set of ordinary differential equations. In this model, the cell proliferation rate and the factor secretion rate depend on matrix stiffness in a sigmoidal function (Michaelis–Menten kinetics), whereas the cell death rate depends on the concentration of soluble factors in a linear function (Fig. 2 *A*, *i*). This model is sufficient to show a biphasic growth pattern with matrix stiffening (*SI Methods*) and simulate the experimental results with AML cells. Two parameters are important: (*i*) potency of factor secretion in response to matrix stiffening [E at half maximal $\delta(E)$: "δE_{50}" in pascals] and (*ii*) potency of cell proliferation in response to matrix stiffening [E at half maximal $\beta(E)$: "βE_{50}" in pascals]. Higher values of these two parameters mean lower sensitivities. Interestingly, increasing δE_{50} alone increases the amplitude of the biphasic curve (Fig. 2 *A*, *ii*), whereas increasing both δE_{50} and βE_{50} shifts the curve to the right (Fig. 2 *A*, *iii*). The curves generated from an analytically derived equation also recapitulate this trend (*SI Methods*). These two results simulate the growth profiles of MOLM-14 and that of U-937, respectively. The results also predict that increasing the RGD ligand density should decrease the sensitivity of factor secretion upon matrix stiffening in MOLM-14 cells, whereas it should decrease both the sensitivity of factor secretion and that of cell proliferation upon matrix stiffening in U-937 cells. Consistent with this model, the conditioned media derived from cells in the matrix at 3 kPa suppress proliferation of AML cells cultured on plastic (Fig. 2*B*), as contrasted to conditioned media from cells cultured in softer gels or on plastic. The cell number at the time of collecting the conditioned media (week 1) remains the same across different conditions (Fig. 1*B*). The results can also be potentially explained by decreased secretion of proliferation promoting factors. Some cytokines are secreted in an autocrine manner to simultaneously regulate both cell growth and death, and this paradoxical regulation can be required to maintain stable steady-state cell concentrations (21). However, mathematically, no biphasic relationship between cell number and matrix stiffness exists in a model when secreted factors directly regulate both cell growth and death rates (*SI Methods*). Although more complex scenarios are possible, the goal here is to identify a parsimonious model to explain the experimental data using a minimal number of variables and functions. The results thus indicate that an autocrine feedback mechanism could regulate the biphasic AML growth induced by matrix stiffening.

Modulation of the Mechanosensitive AML Growth by Inhibition of AKT. AKT becomes more phosphorylated with matrix stiffening (5) and is required for autocrine secretion in some solid tumor cells (22).

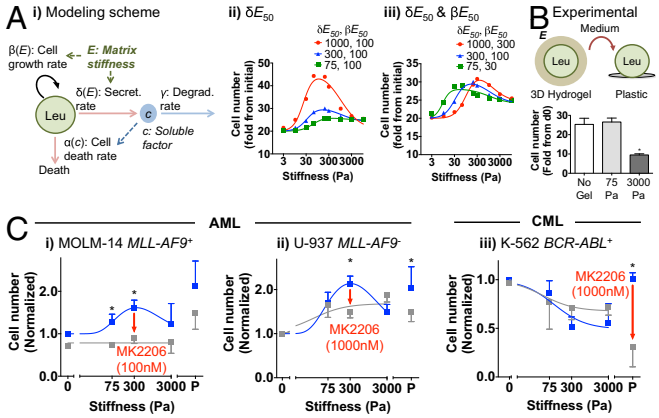

Fig. 2. Matrix stiffness regulates AML cell proliferation through autocrine signaling. (*A*) Simulations by a set of ordinary differentiation equations (*SI Methods*) mimic the biphasic cell proliferation of AML cells. (*i*) A modeling scheme showing an autocrine feedback circuit. $\alpha(c)$, rate of cell death as a function of soluble factor concentration; $\beta(E)$, rate of cell proliferation as a function of E; $\delta(E)$, rate of soluble factor secretion as a function of E; γ, natural decay rate of soluble factors; c, soluble factor concentration; Leu, leukemia cells. The simulation results from (*ii*) increasing δE_{50} alone and (*iii*) increasing both δE_{50} and βE_{50}. The data were fit to biphasic dose–response curves. (*B*) MOLM-14 cells secrete factors that inhibit cell proliferation when cultured in 3D stiff gels. (*Top*) An experimental scheme. (*Bottom*) Total viable cell number after 7 d in the conditioned media from cells in different matrix stiffness. No Gel, 2D culture on plastic. $n = 3$ experiments, $^*P < 0.05$ from one-way ANOVA with Tukey's HSD test, 25 vs. 1,000 Pa. (*C*) Total leukemia cell numbers in 3D hydrogels with or without the presence of the AKT inhibitor MK-2206. The cell numbers from different conditions were normalized against that in the viscous matrix without drug treatment. The whole cell population was used for viability analysis. The data were collected from cells in alginate hydrogels with DS20 RGD. P on the *x* axis, 2D culture on plastic. $n = 4$ experiments, $^*P < 0.05$ from one-way ANOVA with Tukey's HSD test, control vs. MK-2206.

We thus explored whether inhibition of AKT reverses the biphasic AML growth with matrix stiffening. MK-2206 (MK) is an inhibitor against AKT that is in a clinical trial for treatment of solid tumors (23). Interestingly, MK equalizes the number of MOLM-14 across different stiffness at a dose close to IC_{50} (100 nM) (Fig. 2 *C*, *i*). The effect is moderate but significant for U-937 at a higher dose (1,000 nM) (Fig. 2 *C*, *ii*). Consistent with these results, the IC_{50} for suppressing cell proliferation by MK is generally similar regardless of culture environments for AML cells (Fig. S1*B*). Regardless of the basal level of phosphorylated AKT (pAKT) in different AML cells across different matrix stiffness (Fig. S1*C*), MK decreases pAKT in both AML cells with IC_{50} ~50 nM at 300 Pa (Fig. S1*D*). The results thus suggest that AKT inhibition can reverse the matrix stiffness-induced biphasic AML growth because the sensitivity of the AML cells to MK is independent of matrix stiffness.

Matrix Stiffness Modulates Chemosensitivity: Systematic Characterization by Biophysical Screening. In contrast to AML MOLM-14 and U-937 cells, CML K-562 cells become resistant to MK in 3D matrices, whereas they respond to MK on plastic (Fig. 2 *C*, *iii*). Indeed, K-562 cells show 10~20-fold higher IC_{50} values of MK in 3D matrices than on plastic (Fig. S1*B*). Therefore, the same target can exhibit differential chemosensitivity with matrix mechanics in a leukemia cell-type-dependent manner. This motivated broader investigations into how different molecular targets show chemosensitivity as a function of matrix mechanics. To achieve this goal, we first performed dose–response characterization of select drugs against K-562 cells in our screen system. To facilitate this investigation in a high-throughput format, K-562 cells were virally transduced with mCherry and firefly luciferase (Fig. S2*A*). The clone 3 shows similar proliferation kinetics as the whole cell population (Fig. S2*B*) and was used in subsequent studies. Fluorescence signals are linearly proportional to the number of viable cells in hydrogels (Fig. S2*C*).

The tested drugs are either approved by the Food and Drug Administration for treatment of cancers or used to perturb targets involved in mechanotransduction (Table S1). K-562 cells do not respond to two of the tested drugs, including fasudil (Rho-kinase inhibitor) and ruxolitinib (JAK inhibitor). Interestingly, hierarchical clustering analysis of IC_{50} values across different stiffness classifies the remainder of the tested drugs into three categories for K-562 cells (Fig. 3*A*). First, cells become resistant to ~28% of the tested drugs, including doxorubicin and MK, in the RGD ligand-conjugated hydrogel, regardless of matrix stiffness ("class I"). Second, cells are sensitive to ~44% of the drugs, including imatinib, a clinically used inhibitor against CML, and cytosine arabinoside (Ara-C), in a matrix stiffness-dependent manner ("class II"). Third, cells respond to drugs that target the RAF/MAPK pathway (Sorafenib, PD-98059) and the JNK pathway (SP-600125) with similar IC_{50} values across different matrix stiffness ("class III"). Indeed, IC_{50} values are significantly decreased upon matrix stiffening for class II but not for class I and III drugs (Fig. S3*A*). The negative correlation observed with class II drugs is still significant when drugs from all of the classes are combined (Fig. S3*B*). The same trend is also observed with the area under curve (AUC) parameter considering all of the drug classes (Fig. S3*C*), as expected because IC_{50} and AUC generally correlate with each other (24). No significant trend was observed with the Hill slope (m) parameter (Fig. S3*D*), suggesting that potency is a unique parameter that can be used to classify drugs as a function of matrix mechanics.

Dose–response of the same select drugs was also characterized against MOLM-14 cells for systematic comparison with K-562 cells. Hierarchical clustering again classifies these drugs into class I–III for MOLM-14 cells (Fig. 3*B*). Some of the tested drugs belong to different classes with MOLM-14 cells, compared with K-562 cells. Interestingly, MK is a class III drug, whereas drugs against RAF/MAPK and JNK belong to class II with MOLM-14 cells (Fig. 3*B*). The resistance of both K-562 and MOLM-14 cells against their class I and class II drugs was found to depend on the presence of RGD, because the absence of RGD in the hydrogel abolishes differences in IC_{50} between the hydrogel and plastic or across matrix stiffness (Fig. S4*A*). The results thus suggest that *BCR-ABL*$^+$ K-562 cells are sensitive to inhibition of the RAF/MAPK pathway but not the AKT

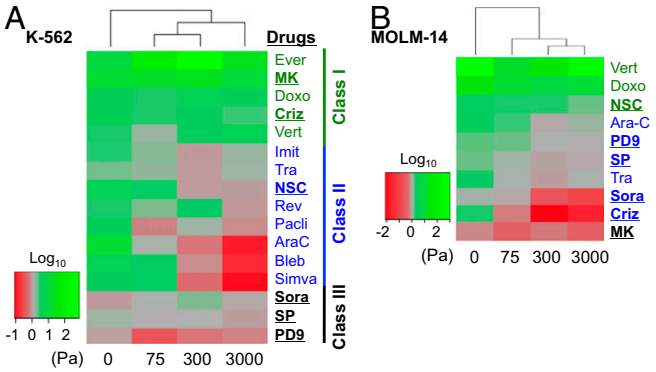

Fig. 3. Matrix stiffness regulates drug sensitivity against distinct targets in myeloid leukemia subtypes. IC_{50} values from (*A*) K-562 cells (clone 3, Fig. S2*B*) and (*B*) MOLM-14 cells (the whole cell population) treated with select drugs (for full name and target pathway of each drug, see Table S1) in 3D hydrogels conjugated with the RGD peptide (DS = 5) were normalized by respective IC_{50} values from plastic, and then log-transformed before hierarchical clustering analysis. Drugs are classified into three classes: class I (ligand sensitive), class II (ligand and matrix stiffness sensitive), and class III (mechanics independent). The data were derived from $n \geq 15$ experiments for *A* and $n \geq 4$ experiments for *B*. Bold, underlined drugs belong to different classes in K-562 and MOLM-14 cells.

pathway, whereas the opposite trend is observed with *MLL-AF9*$^{+}$ MOLM-14 cells.

We thus sought to better understand how gene products that define leukemia subtypes affect the regulation of chemosensitivity by matrix mechanics. A physical interaction network was computationally constructed from a list of experimentally verified protein–protein interactions from curated databases (*SI Methods*). The network shows that BCR and ABL1 proteins interact more directly with the RAF/MAPK pathway components but less with the AKT pathway components (Fig. S4*B*). The opposite trend is observed with AF9 (*MLLT3*) protein. Based on the results in Fig. 3, the network analysis suggests a possibility that *BCR-ABL* and *MLL-AF9* confer sensitivity to RAF/MAPK and AKT inhibitors, respectively, regardless of matrix stiffness. To test this idea, retroviral transduction was used to introduce *BCR-ABL* and *MLL-AF9* to MOLM-14 and K-562 cells, respectively, followed by drug studies. Cells transduced with empty vectors were used as control (Fig. S5*A*). The protein expression level of MLL-AF9 introduced in K-562 cells is comparable to the endogenous level in MOLM-14 cells, whereas the expression level of BCR-ABL in MOLM-14 cells is comparable to the endogenous level in K-562 cells (Fig. S5*B*). *MLL-AF9* significantly increases the sensitivity of K-562 cells against MK across different matrix stiffness (Fig. 4 *A*, *i*), switching the class from I to III (Fig. 3*A*), whereas it does not cause resistance against sorafenib (Fig. 4 *A*, *ii*). However, *BCR-ABL* increases the sensitivity of MOLM-14 cells against sorafenib, switching the class from II to III (Fig. 3*B*), whereas it does not cause resistance against MK (Fig. 4*B*). Therefore, some oncogenes can decouple the dependence of chemosensitivity against specific pathways on matrix ligand or stiffness.

Matrix Stiffness Controls the Growth Kinetics and Resistance to Chemotherapy in Vivo. To evaluate the in vivo relevance of the in vitro results, we used a xenograft model of human extramedullary myeloid leukemias [leukemia cutis (25)] (Fig. 1*A*) by s.c. implanting K-562 cells (clone 3 from Fig. 3*A*) in hydrogel discs with different stiffness into NOD/SCID/IL-2$\gamma^{-/-}$ (NSG) mice (Fig. 5 *A*, *i*). No difference in total viable cell number across different matrix stiffness was observed after cell encapsulation (Fig. S6*A*). Because tumor was not visible by eye for the first 3 wk, bioluminescence live imaging for firefly luciferase in K-562 cells was used to track in vivo growth during this time frame (Fig. 5 *A*, *i*). The in vivo growth follows the first-order kinetics at the natural log scale as described by the classical Gompertz model of tumor growth (26) (Fig. 5 *A*, *ii* and *SI Methods*). Specifically, matrix stiffening decreases both the initial growth rate and the deceleration rate by ∼1.5-fold (Fig. 5 *A*, *iii* and *iv*), and hence maintains a constant maximal tumor signal (i.e., plateau = growth/deceleration). The results are consistent with the in vitro growth kinetics measured for 2 wk (Fig. S6*B*). The in vivo cell number in soft matrix is up to ∼100-fold higher than that in stiff matrix at 2 wk (*SI Methods*), and the difference gradually diminishes afterward (Fig. S6*C*). Therefore, initial matrix stiffening leads to both delayed and sustained cancer growth in vivo.

We then tested whether soft matrix confers resistance to standard chemotherapy in vivo as observed the in vitro drug screen studies. After 1-wk implantation, a myelosuppresive dose of Ara-C [62.5mg/kg (27)] was intraperitoneally administered daily into each mouse for 3 wk (Fig. 5 *B*, *i*). Interestingly, fitting the bioluminescence data for the first 3 wk shows that Ara-C suppresses the cell growth in the stiff matrix predominantly by increasing deceleration rate (∼2.5-fold) rather than decreasing initial growth rate (Fig. 5 *B*, *ii*). In fact, initial growth rate in stiff matrix is increased slightly by ∼1.4-fold after Ara-C (Fig. S6 *D*, *i*). It is thus estimated that Ara-C decreases the plateau of the tumor signal in the stiff matrix by ∼1.6-fold (Fig. S6 *D*, *i*). In contrast, cells are resistant to Ara-C in the soft matrix (Fig. S6 *D*, *ii*). To confirm these results, we investigated whether the treatment affects tumor growth at later time points after the withdrawal for 2 wk. An overall tumor volume rather than bioluminescence was measured

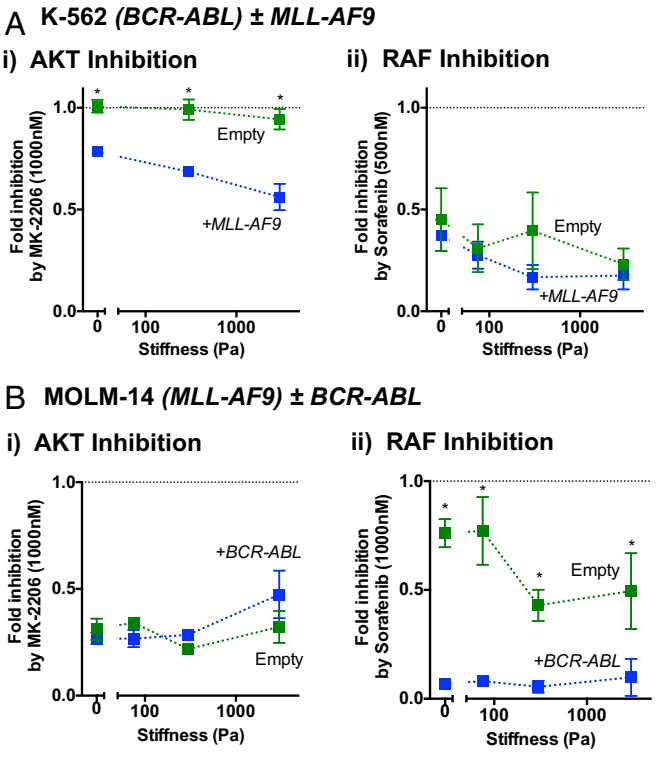

Fig. 4. Leukemic oncogenes decouple the dependence of chemosensitivity on integrin ligands and matrix stiffness. (*A*) Overexpression of *MLL-AF9* into K-562 cells increases their sensitivity against MK-2206 (AKT inhibitor) (*i*) but does not affect the sensitivity against sorafenib (RAF inhibitor) (*ii*) across different matrix stiffnesses. (*B*) Overexpression of *BCR-ABL* into MOLM-14 cells does not alter their sensitivity against MK-2206 (*i*) but increases the sensitivity against sorafenib (*ii*). The whole cell population was used for viability analysis. **P* < 0.05, paired *t* test between empty oncogene vectors. *n* = 3 experiments. Error bars indicate ± SEM.

at week 6 (*SI Methods*), because bioluminescence signals become saturated at week 4 (Fig. S6*E*). The tumor volume remains higher in soft than in stiff matrix at week 6, with the difference less than an order of magnitude (Fig. 5 *B*, *iii*). Consistent with the prediction from the earlier time points (Fig. S6 *D*, *i*), Ara-C decreases the volume of tumors originating from stiff but not soft matrix (Fig. 5 *B*, *iii*), in a dose-dependent manner (Fig. S6*F*).

Considering that the diameter of leukemia cells is ∼10 μm, the initial 1 million implanted K-562 cells per 20 μL gel disk occupies ∼2.5% of the total gel volume. This means that after 1 wk, when the tumor luminescence is increased by >40 fold (Fig. 5*A*), the cell number reaches the limit of the initial scaffold volume. Indeed, histological analyses after 2 wk from the implantation show that both blood and stromal-like cells are present with gel fragments, suggesting both donor cell overgrowth and host cell infiltration (Fig. S7*A*). This could be explained by stress relaxation of hydrogels followed by the loss of structural integrity, which is typical of ionically cross-linked hydrogels as cells proliferate (28). Histological observations suggest a qualitative trend where fewer stromal-like cells may be present with Ara-C compared with vehicle control, but more dead hematopoietic cells are visible in stiff matrices compared with soft (Fig. S7*B*). This is likely due to increased apoptosis, as indicated by increased cleaved caspase-3 staining (Fig. S8*A*). To characterize mechanobiological features further, we performed immunofluorescence studies on implanted K-562 cells. Whereas nonhuman stromal-like cells generally express higher yes-associated protein (YAP), a mechanosensitive transcription factor (29), than human K-562 cells, YAP^{+} human cells are more visible in the stiff matrix compared with the soft matrix (Fig. S8*B*). No difference was observed in F-actin distribution. Ara-C

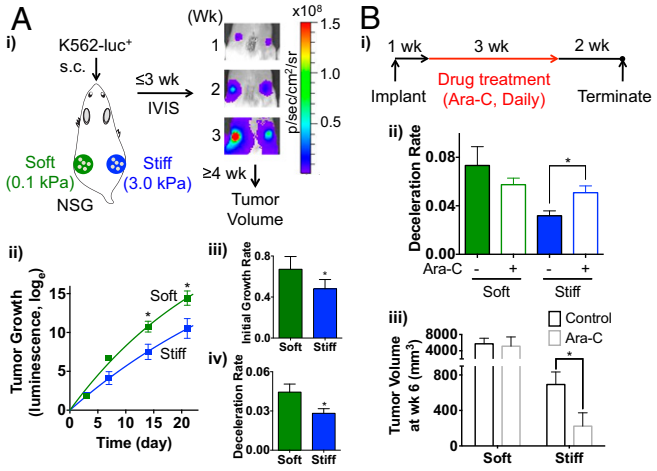

Fig. 5. Resistance of leukemia cells against conventional chemotherapy in soft matrix in vivo. (*A*) Matrix stiffness affects K-562 (clone 3) cell growth in vivo. (*i*) Experimental scheme and representative images showing tumor growth from soft and stiff matrix in the human xenograft extramedullary leukemia model. (*ii*) Tumor growth for the first 3 wk after implantation described by first-order kinetics based on luminescence signals (normalized to Y0; see *SI Methods*). (*iii*) Mean initial growth rate. (*iv*) Mean deceleration rate. $n = 15$ mice, three experiments, $^*P < 0.01$, paired t test. (*B*) CML cells are resistant to Ara-C in soft matrix. (*i*) Experimental scheme. (ii) Ara-C increases deceleration rate in stiff but not in soft matrix. (iii) Ara-C decreases tumor volume at week 6 in stiff but not in soft matrix. $n = 6$ mice, two experiments, $^*P < 0.01$ from one-way ANOVA with Tukey's HSD test, stiff control vs. treated.

does not seem to alter these trends. Together, the results show that initial matrix softening increases resistance against standard chemotherapy.

Discussion

A variety of molecular signals emanating from stromal cells in the BM microenvironment are known to play important roles in modulating tumor survival and drug sensitivity. The use of tumor–stroma coculture systems to identify new small-molecule inhibitors against tumor cells highlights the importance of recapitulating different components of the microenvironment to discover next-generation cancer therapies. Prior efforts have primarily focused on incorporating molecular and cellular components into in vitro drug screens on culture plastic. We demonstrate that engineering biophysical factors of the microenvironment, especially 3D matrix stiffness, into a quantitative, high-throughput screen format (Fig. 1*A*) reveals systematic variations in proliferation and drug responses of myeloid leukemias.

Matrix stiffening initially enhances the proliferation of MOLM-14 and U-937 cells but suppresses that of K-562 cells (Fig. 1*B*). This result mirrors the previous observation that TGF-β1 secreted from parathyroid hormone receptor-stimulated osteoblasts in vivo enhances *MLL-AF9*$^+$ AML proliferation but attenuates *BCR-ABL*$^+$ CML (3). Because TGF-β1 also regulates leukemia cells in an autocrine manner (30), it is possible that physical cues differentially regulate the proliferation of myeloid leukemia subtypes through the autocrine secretion of TGF-β. In addition, cell-generated mechanical tension resulting from matrix stiffening may increase release of matrix-bound active TGF-β (31). In contrast to K-562, the effect of stiffness on growth of MOLM-14 and U-937 is biphasic, suggesting the presence of other autocrine factors secreted specifically in stiffer matrices that suppress proliferation (Fig. 2 *A* and *B*). Delineating the interplay between specific growth factors and physical cues will thus be important to understand how matrix stiffness in the tumor microenvironment differentially regulates myeloid leukemias with distinct mutations.

Although a number of molecular targets are known to be involved in matrix stiffness sensing, most previous studies were performed with compounds at a single concentration. However, this approach does not reveal whether drug sensitivity against each target is influenced by matrix mechanics. This is an important consideration, because for drug targets whose inhibition depends on matrix stiffness a very high dose needs to be used to achieve similar efficacies in different physical environments, and this could increase the risk of off-target effects and toxicity. For instance, blebbistatin, an inhibitor against the myosin-II motor, at a high dose is known to eliminate differences in cellular functions and phenotypes caused by changes in matrix stiffness (5). However, higher concentrations of blebbistatin show off-target effects in some myosin-II mutant cells (32). Indeed, our results suggest that matrix stiffness modulates the sensitivity of cells against blebbistatin (Fig. 3*A*). Our 3D screen approach thus helps delineate how drug actions against different targets depend on mechanical cues for individual cancer subtypes, which could then further allow the identification of compounds that can potently target cells regardless of their physical environments.

It has been suggested that the tumor microenvironment induces the dormancy of leukemia cells, and hence they become more resistant to anticancer drugs due to slow proliferation (33). However, increasing evidence suggests that the cytotoxic effects of chemotherapeutic agents are not likely dependent on proliferation in human tumors (34). Indeed, adhesion of AML cells to matrix or stromal cells is known to decrease chemosensitivity, regardless of alterations in proliferation rates (35). Consistent with this notion, no clear correlation was observed between cell proliferation and drug sensitivity in our screen. In addition, although K-562 growth is independent of RGD (Fig. 1*B*) it mediates chemosensitivity regulated by matrix mechanics (Fig. S4*A*). Therefore, chemosensitivity may not always be a function of cell proliferation in pathophysiological contexts, providing evidence against the antiproliferative hypothesis.

We demonstrate the utility of implanting the same hydrogels used in an in vitro screen into xenograft models to bridge the gap between in vitro and in vivo preclinical studies. Although it is presently difficult to control matrix stiffness orthotopically in BM for systemic leukemia models, s.c. implantation models the extramedullary manifestation of leukemias, which often predicts rapid disease progression and poor prognosis in advanced-stage patients (36). Even though in vivo tumor growth is a complex process that involves angiogenesis and matrix remodeling after implantation, the impact of stiffness on growth kinetics parameters of K-562 cells in vitro (Fig. S6*B*) are consistent with those in vivo (Fig. 5*A*). This suggests that matrix stiffness is a dominant parameter that regulates tumor growth.

The s.c. xenograft model can also be used to study drug resistance against human leukemias, because chemotherapy adequate to induce marrow remission does not always control the extramedullary sites due to a high probability of relapse (25). Indeed, the dose of Ara-C used in previous studies to control systemic leukemias (6.25 mg/kg) (37) is not sufficient to induce regression in s.c. sites (Fig. S6*F*). Upon dose escalation, leukemia cells become more sensitive to standard chemotherapy in the stiff matrix (Fig. 5*B*) where cells grow slowly but steadily (Fig. 5*A*), again providing evidence against the antiproliferative hypothesis. In contrast to previous studies with 2D plastic culture, Ara-C acts on leukemias originating from the stiff matrix by increasing the deceleration rate rather than decreasing the growth rate, suggesting involvement of additional mechanisms in its tumor effect in vivo. One possible explanation is that Ara-C increases apoptosis (Fig. S8*A*), giving rise to augmented compensatory proliferation of surviving cells (Fig. S6 *D*, *i*), as previously observed in chemical hepatocarcinogenesis (38).

YAP is relatively low in hematopoietic cells compared with other cell types (Fig. S8*B*) (18), and this could explain why leukemia cells are generally resistant to a YAP inhibitor alone (Fig. 3). Although a functional significance of YAP up-regulation in in vivo implanted K-562 cells upon matrix stiffening (Fig. S8*B*) remains to be determined, it was previously shown that YAP overexpression

increases cisplatin-induced apoptosis of breast cancer cells in the presence of p73, which is activated by DNA damage (39). The results thus suggest a possibility that up-regulation or increased nuclear localization of YAP upon matrix stiffening (29) may sensitize some leukemia cells against chemotherapeutic drugs that target DNA.

Overall, we present a combined biophysical screening and in vivo validation workflow that could be applied to a range of cancers to reveal their growth kinetics and pharmacodynamics profiles as a function of physical environments. The resistance of leukemia cells against standard chemotherapy with matrix softening underscores the utility of this quantitative approach for investigating physically induced cellular drug resistance and discovering molecular targets that can be potentially modulated across different mechanical environments.

Methods

Cell culture, mechanical characterization of hydrogels, in vivo tumor growth studies, mathematical modeling, and other standard techniques are described in *SI Methods*. All animal work was performed in compliance with NIH and the ethical committee from Harvard University.

For chemical screen in hydrogels, cells in culture were washed two times, followed by resuspension in the serum-free Fluorobrite DMEM media. Cells were then mixed with the alginate solution to make the final gel concentration of 1%. Eighty microliters of the cell–alginate mixture was then deposited into each well of a 96-well plate (U-Bottom; Corning) that contained different concentrations of 5× calcium sulfate (20 μL). Immediately after deposition, the content was rapidly mixed by swirling with pipette tips and pipetting up and down ∼10 times. The plate was then incubated at 37 °C for 2 h to allow gels to form, and 100 μL of phenol red-free RPMI with 10% FBS was added on top of each gel; 1,000–10,000 cells were plated per well. Dose–response curves at day 7 were obtained for 20 drugs titrated at five or more doses (1/3∼1/10 serial dilutions) (Table S1). The proliferation of unlabeled cells was measured by alamarBlue (Invitrogen), and that of mCherry$^+$ cells was measured by reading fluorescence signals (emission 587 nm and excitation 620 nm).

ACKNOWLEDGMENTS. We thank Dr. Andre Kajdascsy-Balla (Department of Pathology, University of Illinois at Chicago College of Medicine) for providing an expert pathological review of histological images from tumors. We thank Dr. David Scadden for invaluable comments on the manuscript and Dr. David Sykes for providing reagents (Massachusetts General Hospital). This work was supported by National Institutes of Health Grants RO1EB014703 (to D.J.M.) and R00HL125884 (to J.-W.S.).

1. Daley GQ (2004) Chronic myeloid leukemia: Proving ground for cancer stem cells. *Cell* 119(3):314–316.
2. Krivtsov AV, Armstrong SA (2007) MLL translocations, histone modifications and leukaemia stem-cell development. *Nat Rev Cancer* 7(11):823–833.
3. Krause DS, et al. (2013) Differential regulation of myeloid leukemias by the bone marrow microenvironment. *Nat Med* 19(11):1513–1517.
4. Cheng JQ, Lindsley CW, Cheng GZ, Yang H, Nicosia SV (2005) The Akt/PKB pathway: Molecular target for cancer drug discovery. *Oncogene* 24(50):7482–7492.
5. Chaudhuri O, et al. (2014) Extracellular matrix stiffness and composition jointly regulate the induction of malignant phenotypes in mammary epithelium. *Nat Mater* 13(10):970–978.
6. Paszek MJ, et al. (2005) Tensional homeostasis and the malignant phenotype. *Cancer Cell* 8(3):241–254.
7. Holst J, et al. (2010) Substrate elasticity provides mechanical signals for the expansion of hemopoietic stem and progenitor cells. *Nat Biotechnol* 28(10):1123–1128.
8. Shin JW, et al. (2014) Contractile forces sustain and polarize hematopoiesis from stem and progenitor cells. *Cell Stem Cell* 14(1):81–93.
9. Kenny HA, et al. (2015) Quantitative high throughput screening using a primary human three-dimensional organotypic culture predicts in vivo efficacy. *Nat Commun* 6:6220.
10. Yoshii Y, et al. (2015) High-throughput screening with nanoimprinting 3D culture for efficient drug development by mimicking the tumor environment. *Biomaterials* 51: 278–289.
11. Nguyen TV, Sleiman M, Moriarty T, Herrick WG, Peyton SR (2014) Sorafenib resistance and JNK signaling in carcinoma during extracellular matrix stiffening. *Biomaterials* 35(22):5749–5759.
12. Schrader J, et al. (2011) Matrix stiffness modulates proliferation, chemotherapeutic response, and dormancy in hepatocellular carcinoma cells. *Hepatology* 53(4):1192–1205.
13. Liu J, et al. (2012) Soft fibrin gels promote selection and growth of tumorigenic cells. *Nat Mater* 11(8):734–741.
14. Shin JW, et al. (2013) Lamins regulate cell trafficking and lineage maturation of adult human hematopoietic cells. *Proc Natl Acad Sci USA* 110(47):18892–18897.
15. Huebsch N, et al. (2010) Harnessing traction-mediated manipulation of the cell/matrix interface to control stem-cell fate. *Nat Mater* 9(6):518–526.
16. Gurkan UA, Akkus O (2008) The mechanical environment of bone marrow: A review. *Ann Biomed Eng* 36(12):1978–1991.
17. Zhao X, Huebsch N, Mooney DJ, Suo Z (2010) Stress-relaxation behavior in gels with ionic and covalent crosslinks. *J Appl Phys* 107(6):63509.
18. Swift J, et al. (2013) Nuclear lamin-A scales with tissue stiffness and enhances matrix-directed differentiation. *Science* 341(6149):1240104.
19. Hemler ME, Huang C, Schwarz L (1987) The VLA protein family. Characterization of five distinct cell surface heterodimers each with a common 130,000 molecular weight beta subunit. *J Biol Chem* 262(7):3300–3309.
20. Dias S, et al. (2000) Autocrine stimulation of VEGFR-2 activates human leukemic cell growth and migration. *J Clin Invest* 106(4):511–521.
21. Hart Y, Antebi YE, Mayo AE, Friedman N, Alon U (2012) Design principles of cell circuits with paradoxical components. *Proc Natl Acad Sci USA* 109(21):8346–8351.
22. Chen CC, et al. (2012) Autocrine prolactin induced by the Pten-Akt pathway is required for lactation initiation and provides a direct link between the Akt and Stat5 pathways. *Genes Dev* 26(19):2154–2168.
23. Yap TA, et al. (2011) First-in-man clinical trial of the oral pan-AKT inhibitor MK-2206 in patients with advanced solid tumors. *J Clin Oncol* 29(35):4688–4695.
24. Fallahi-Sichani M, Honarnejad S, Heiser LM, Gray JW, Sorger PK (2013) Metrics other than potency reveal systematic variation in responses to cancer drugs. *Nat Chem Biol* 9(11):708–714.
25. Cho-Vega JH, Medeiros LJ, Prieto VG, Vega F (2008) Leukemia cutis. *Am J Clin Pathol* 129(1):130–142.
26. Norton L, Simon R, Brereton HD, Bogden AE (1976) Predicting the course of Gompertzian growth. *Nature* 264(5586):542–545.
27. Zuber J, et al. (2009) Mouse models of human AML accurately predict chemotherapy response. *Genes Dev* 23(7):877–889.
28. Desai RM, Koshy ST, Hilderbrand SA, Mooney DJ, Joshi NS (2015) Versatile click alginate hydrogels crosslinked via tetrazine-norbornene chemistry. *Biomaterials* 50: 30–37.
29. Dupont S, et al. (2011) Role of YAP/TAZ in mechanotransduction. *Nature* 474(7350): 179–183.
30. Ruscetti FW, Akel S, Bartelmez SH (2005) Autocrine transforming growth factor-beta regulation of hematopoiesis: many outcomes that depend on the context. *Oncogene* 24(37):5751–5763.
31. Wipff PJ, Rifkin DB, Meister JJ, Hinz B (2007) Myofibroblast contraction activates latent TGF-beta1 from the extracellular matrix. *J Cell Biol* 179(6):1311–1323.
32. Shu S, Liu X, Korn ED (2005) Blebbistatin and blebbistatin-inactivated myosin II inhibit myosin II-independent processes in Dictyostelium. *Proc Natl Acad Sci USA* 102(5): 1472–1477.
33. Ishikawa F, et al. (2007) Chemotherapy-resistant human AML stem cells home to and engraft within the bone-marrow endosteal region. *Nat Biotechnol* 25(11):1315–1321.
34. Mitchison TJ (2012) The proliferation rate paradox in antimitotic chemotherapy. *Mol Biol Cell* 23(1):1–6.
35. Matsunaga T, et al. (2003) Interaction between leukemic-cell VLA-4 and stromal fibronectin is a decisive factor for minimal residual disease of acute myelogenous leukemia. *Nat Med* 9(9):1158–1165.
36. Ansell LH, Mehta J, Cotliar J (2013) Recurrent aleukemic leukemia cutis in a patient with pre-B-cell acute lymphoblastic leukemia. *J Clin Oncol* 31(20):e353–e355.
37. Hu S, et al. (2011) Activity of the multikinase inhibitor sorafenib in combination with cytarabine in acute myeloid leukemia. *J Natl Cancer Inst* 103(11):893–905.
38. Maeda S, Kamata H, Luo JL, Leffert H, Karin M (2005) IKKbeta couples hepatocyte death to cytokine-driven compensatory proliferation that promotes chemical hepatocarcinogenesis. *Cell* 121(7):977–990.
39. Basu S, Totty NF, Irwin MS, Sudol M, Downward J (2003) Akt phosphorylates the Yes-associated protein, YAP, to induce interaction with 14-3-3 and attenuation of p73-mediated apoptosis. *Mol Cell* 11(1):11–23.
40. Rowley JA, Madlambayan G, Mooney DJ (1999) Alginate hydrogels as synthetic extracellular matrix materials. *Biomaterials* 20(1):45–53.
41. He Y, et al. (2002) The coiled-coil domain and Tyr177 of bcr are required to induce a murine chronic myelogenous leukemia-like disease by bcr/abl. *Blood* 99(8):2957–2968.
42. Euhus DM, Hudd C, LaRegina MC, Johnson FE (1986) Tumor measurement in the nude mouse. *J Surg Oncol* 31(4):229–234.
43. Saito R, et al. (2012) A travel guide to Cytoscape plugins. *Nat Methods* 9(11): 1069–1076.

Supporting Information

Shin and Mooney 10.1073/pnas.1611338113

SI Methods

Cell Lines and Reagents. Human myeloid leukemia cell lines (MOLM-14, U-937, and K-562) and a retroviral construct with *MLL-AF9* gene were kindly provided by the laboratory of David Scadden, Massachusetts General Hospital, Boston. These cell lines are also available from commercial vendors, such as American Type Culture Collection. Cells were cultured in RPMI, 1% penicillin and streptomycin, and 10% (vol/vol) FBS at 37 °C in 5% (or 50,000 ppm) CO_2. All drugs were obtained from LC chemicals except Cytarabine (Ara-C) from Sigma, Everolimus from Cell Signaling Technology, and MK-2206 from Biovision. All of the antibodies were purchased from Cell Signaling Technology. Phenol red-free DMEM (Fluorobrite) was purchased from Invitrogen.

Hydrogel Preparation and Mechanical Characterizations. Sodium alginate with a low molecular weight (LF10/60) was purchased from FMC Biopolymer and prepared as described previously (40). Briefly, alginate was dialyzed against deionized water for 3 d (molecular weight cutoff of 3,500 Da), filtered with activated charcoal, sterile-filtered, and lyophilized. It was then reconstituted in serum-free, phenol red-free DMEM at 4% (wt/vol) as a stock dilution. In some cases, an RGD peptide (GGGGRGDSP; Peptides International) was conjugated to alginate using carbodiimide chemistry at concentrations such that 5 or 20 RGD peptides were coupled to 1 alginate polymer on average. The coupling efficiency was previously characterized (40). The gels were formed by mixing alginate with different concentrations of calcium sulfate. The mechanical properties of alginate hydrogels were characterized with an AR-G2 stress-controlled rheometer (TA Instruments) by directly depositing them onto the surface plate of the rheometer. A 20-mm plate was brought down before the alginate started to gel, and the mechanical properties were then measured over time, with the storage modulus recorded at 0.5% strain and at 1 Hz. The storage modulus at these settings was measured to range from 25 to 1,000 Pa, which corresponds to Young's modulus ranging from 75 to 3,000 Pa, using the equations $E=2G(1+\upsilon)$ and $G=\sqrt{G'^2+G''^2}$, where E = Young's modulus, υ is Poisson's ratio of 0.5, G is the shear modulus, G' is the shear storage modulus, and G'' is the shear loss modulus.

Establishing Cell Lines That Express Exogenous Genes. To introduce mCherry and firefly luciferase in leukemia cells, lentiviral particles containing the vector with mCherry-IRES-firefly luciferase driven by the CMV promoter were purchased from the Vector Core at Massachusetts General Hospital. Cells were incubated with viral particles for 2 d. Single cells expressing mCherry were then sorted into 96-well plates via flow-activated cell sorting (FACS). Individual clones were expanded for 14 d. Clones were selected for further in vitro and in vivo analyses according to proliferation kinetics and intensity of fluorescence and luminescence signals. For *MLL-AF9* transduction, retroviral particles were obtained by co-transfecting the vector containing *MLL-AF9* or no gene ("empty") with the neomycin resistance gene and the packaging vector into Human Embryonic Kidney (HEK)-293 cells, followed by collection of supernatant at days 2–3 and ultracentrifugation through Amicon Ultra-15 (3-kDa cutoff ; Millipore) filters to concentrate particles. After introducing particles into leukemia cells, they were treated with G-418 (Invitrogen) to select for virally transduced cells. For *BCR-ABL* transduction, nerve growth factor receptor (NGFR) P210 (plasmid 27486) was a gift from Warren Pear, Addgene, Cambridge, MA, along with NGFR empty vector (plasmid 27489; Addgene) as previously published (41). Retroviral particles were obtained and used for transduction in a fashion similar to *MLL-AF9*. After transduction, NGFR-positive cells were sorted by FACS and expanded. The sorting and expansion cycle was repeated two to three times to achieve >95% of NGFR-positive cells for drug studies.

Tumor Growth Studies in Localized Xenograft Extramedullary Leukemia Models. All animal experiments were performed in compliance with NIH and institutional guidelines approved by the ethical committee from Harvard University. K-562 cells (10^6) expressing mCherry and firefly luciferase were encapsulated in a 5-mm diameter × 1-mm height alginate gel disk (~20 μL). A pair of gel discs with E = 100 or 3,000 Pa was s.c. implanted into each flank of 8- to 12-wk-old NOD/SCID/IL-2$\gamma^{-/-}$ mice. To monitor in vivo tumor growth over time, 3 mg D-luciferin was injected intraperitoneally into the 25-g mice followed by luminescence imaging with the IVIS Spectrum (PerkinElmer) within 30 min of injection. Average radiance (photons per second per centimeter squared per steradian) from each time point was measured from each implant for the first 3 wk. Beyond this time point, bioluminescence becomes saturated (Fig. S6*E*), and tumor volume was assessed using calipers by the modified ellipsoid formula: 1/2 × (length × width^2) (42).

Hierarchical Clustering Analysis. Before analysis, dose–response parameters, including IC_{50} and AUC values, of each drug from different stiffnesses were normalized against their respective values on plastic followed by log transformation. m values were not normalized. The complete linkage method with Euclidean distance measure was implemented using R (heatmap.2 function; https://www.r-project.org/) to perform hierarchical clustering of the dose–response data.

Intracellular Flow Cytometry. Cells were retrieved from cross-linked hydrogels by digesting with alginate lyase (3.4 mg/mL) for 15 min at 37 °C. Cell suspensions were then immediately fixed with 4% (wt/vol) paraformaldehyde for 10 min, followed by washing two times with PBS/0.1% BSA. Cells were then washed and resuspended in the staining media (PBS/0.1% saponin). Primary antibodies against total AKT and pAKT (Ser-473) were added to cells at 1:100 dilution along with Hoechst 33342 at 1:5,000 dilution. Cells were incubated at room temperature for 2 h. They were then washed with PBS and incubated with secondary antibodies (Alexa 647 anti-rabbit and Alexa 488 anti-mouse) for 30 min, followed by resuspension in PBS. Flow cytometry analysis was done using LSR II (BD).

Correlation Analysis. To observe relationships between Gompertz growth parameters and doses (normalized by IC_{50} values on plastic) in different matrix stiffnesses, Spearman correlation analyses were performed using GraphPad Prism 6. In some cases where cells were treated with higher drug doses the data could not be fitted to the Gompertz kinetics because cells did not proliferate significantly over time, and therefore they were excluded from correlation analysis. A correlation is considered statistically significant if $P < 0.05$.

Curve Fitting. The pharmacodynamics data were fitted to the logistical sigmoidal function

$$Y = Max + \frac{(Min - Max)}{1 + \left(\frac{IC_{50}}{X}\right)^m},$$

where Y is the cell number at dose X, Max and Min are the top and bottom asymptotes of the response, respectively, IC_{50} is the

concentration at half-maximal effect (potency), and m is the Hill slope. Constraints are $Min = 0$ (i.e., absolute IC_{50}) and $m > 0$. Area under dose–response curve (AUC) values were calculated over five doses using the trapezoid rule. Nonlinear least-squares regression was performed in GraphPad Prism 6. More than 90% of all of the dose–response data followed the sigmoidal model with $R^2 > 0.7$ and were used for further analyses.

Effects of matrix stiffening on AML cell number were fitted to the biphasic curve function

$$Y = Max + \frac{Init - Max}{1 + 10^{(\mathrm{Log}EC_{50} - E)\cdot m1}} + \frac{Final - Max}{1 + 10^{(E - \mathrm{Log}IC_{50})\cdot m2}},$$

Where Y is the cell number at stiffness X (log scale), *Init*, *Final*, and *Max* are the cell numbers at the initial, final, and maximum plateau phases, respectively, EC_{50} is the stiffness at half-maximal effect when cell number increases, IC_{50} is the stiffness at half-maximal effect when cell number decreases, and *m1* and *m2* are Hill slopes.

Cell Proliferation Kinetics Curve Fitting. The Gompertz function is defined as follows:

$$\frac{dN(t)}{dt} = K1 \cdot G(t) \cdot N(t)$$

$$\frac{dG(t)}{dt} = -K2 \cdot G(t),$$

where $N(t)$ is the cell number at time t, $K1{\cdot}G(t)$ is the growth rate at time t [i.e., $K1{\cdot}G(0)$ is the initial growth rate], and $K2$ is the deceleration rate. These differential equations can be solved analytically, resulting in the following equation:

$$N(t) = N(0) \cdot e^{\left(\frac{K1\cdot G(0)}{K2}\right)\cdot\left(1 - e^{-K2\cdot t}\right)}.$$

This equation was used to fit the cell proliferation kinetics data at different doses and different stiffnesses. Nonlinear least-squares regression was performed in GraphPad Prism 6. More than 70% of all of the proliferation kinetics data followed this model with $R^2 > 0.7$ and were used for further analyses.

Transforming $N(t)$ to the natural log scale will lead to the first-order growth kinetics equation:

$$\ln\left(\frac{N(t)}{N(0)}\right) = \frac{K1 \cdot G(0)}{K2} \cdot \left(1 - e^{-K2\cdot t}\right).$$

The log scale data from the in vivo tumor growth analysis for the first 3 wk were fit to this equation. For each fit, a Y-intercept was extrapolated, and each value was subtracted from the Y-intercept to correct for the background signal. Bioluminescence signals become saturated at week 4 (Fig. S6*E*), and hence the data beyond this time point were not used for fitting.

One way to compare luminescence signals between soft and stiff matrices is

$$Y = \frac{\ln(AX)}{\ln(X)} = \frac{\ln(A)}{\ln(X)} + 1,$$

where A is the fold difference in luminescence between soft and stiff, Y is the ratio between soft and stiff at the natural log scale, and X is the raw luminescence signal of the stiff matrix. Therefore,

$$A = e^{(Y-1)\ln(X)}.$$

For example, at week 2 when $X = 316.2$ and $Y = \sim 1.8$, A is ~100 (Fig. S6*C*).

Modeling an Autocrine Feedback Circuit of AML Cell Proliferation Modulated by Matrix Stiffening. We constructed a simple set of differential equations to describe an autocrine feedback circuit (Fig. 2 *B*, *i*) as follows:

$$\frac{dL}{dt} = \beta(E)L - \alpha(c)L \qquad \textbf{[S1]}$$

$$\frac{dc}{dt} = \delta(E)L - \gamma c, \qquad \textbf{[S2]}$$

where L is the number of leukemia cells at time t, c is the concentration of factors secreted from cells at time t, $\beta(E)$ is the rate of proliferation at matrix stiffness E, $\delta(E)$ is the rate of factor secretion at E, $\alpha(c)$ is the cell death rate at c, and γ is the factor degradation rate. These equations were solved computationally using MATLAB (MathWorks) with the function ode45 and the following values: $\gamma = 0.5$, $\alpha(c) = c$.

$$\beta(E) = \frac{m_\beta}{1 + \left(\frac{\beta E_{50}}{E}\right)^{k_\beta}}, \qquad \textbf{[S3]}$$

where βE_{50} is the E at half-maximal proliferation rate, m_β is the maximal proliferation rate, and k_β is the Hill coefficient of the proliferation rate.

$$\delta(E) = \frac{m_\delta}{1 + \left(\frac{\delta E_{50}}{E}\right)^{k_\delta}}, \qquad \textbf{[S4]}$$

where δE_{50} is the E at half-maximal factor secretion rate, m_δ is the maximal secretion rate, and k_δ is the Hill coefficient of the secretion rate.

To solve these equations analytically, at the steady state (ss), $dL/dt = 0$ and $dc/dt = 0$, and hence:

From Eq. **S1**:

$$\beta(E) = \alpha(c) = c_{ss}.$$

From Eq. **S2**:

$$\delta(E)L_{ss} = \gamma c_{ss}.$$

After substituting c_{ss} with $\beta(E)$,

$$\delta(E)L_{ss} = \gamma\beta(E)$$

$$L_{ss} = \frac{\gamma\beta(E)}{\delta(E)}$$

$$L_{ss} = \left(\frac{\gamma \cdot m_\beta}{m_\delta}\right)\frac{\left(1 + \left(\frac{\delta E_{50}}{E}\right)^{k_\delta}\right)}{\left(1 + \left(\frac{\beta E_{50}}{E}\right)^{k_\beta}\right)} = \left(\frac{\gamma \cdot m_\beta}{m_\delta}\right)\frac{E^{k_\beta}\left(E^{k_\delta} + \delta E_{50}{}^{k_\delta}\right)}{E^{k_\delta}\left(E^{k_\beta} + \beta E_{50}{}^{k_\beta}\right)}. \qquad \textbf{[S5]}$$

Plotting L_{ss} vs. E of Eq. **S5** with the initial $L_{ss} = 20$, $\gamma = 0.5$, $m_\beta = 10$, $m_\delta = 1$, $k_\beta = 2$, $k_\delta = 1$ shows

different biphasic curves with varied δE_{50} and βE_{50} as in Fig. 2*A*. Also, the equation suggests that the cell number will reach plateau with high E at

$$\lim_{E\to\infty} L_{ss} = \frac{\gamma \cdot m_\beta}{m_\delta}.$$

Analysis of an Alternative Model. Although the model in Fig. 2*A* considers when the proliferation rate is a function of matrix stiffness, and the death rate is a function of the secreted factors, it is possible that both proliferation and death rates directly depend on secreted factors as shown previously (21).

$$\frac{dL}{dt} = \beta(c)L - \alpha(c)L \quad \textbf{[S6]}$$

$$\frac{dc}{dt} = \delta(E)L - \gamma c \quad \textbf{[S7]}$$

$$\beta(c) = \frac{m_\beta}{1 + \left(\frac{\beta c_{50}}{c}\right)^{k_\beta}}, \quad \textbf{[S8]}$$

where βc_{50} is the c at half-maximal proliferation rate, m_β is the maximal proliferation rate, and k_β is the Hill coefficient of the proliferation rate.

$$\delta(E) = \frac{m_\delta}{1 + \left(\frac{\delta E_{50}}{E}\right)^{k_\delta}}, \quad \textbf{[S9]}$$

where δE_{50} is the E at half-maximal factor secretion rate, m_δ is the maximal secretion rate, and k_δ is the Hill coefficient of the secretion rate.

At the steady state (ss), $dL/dt = 0$ and $dc/dt = 0$:

From Eq. **S6**, given $\alpha(c) = c$:

$$\beta(c) = \alpha(c)$$

$$\frac{m_\beta}{1 + \left(\frac{\beta c_{50}}{c_{ss}}\right)^{k_\beta}} = c_{ss}. \quad \textbf{[S10]}$$

This suggests that c_{ss} is independent of L or E.

As in Eq. **S5**, consider the case when $m_\beta = 10$ and $k_\beta = 2$. Rearranging Eq. **S10** leads to a quadratic equation:

$$c_{ss}{}^2 - 10c + \beta c_{50}{}^2 = 0. \quad \textbf{[S11]}$$

Solving Eq. S11 leads to

$$c_{ss} = 5 - \sqrt{25 - \beta c_{50}{}^2}\,. \quad \textbf{[S12]}$$

Because $25 - \beta c_{50}{}^2 \geq 0$,

$$0 \leq c_{ss} \leq 5.$$

From Eq. **S7**, given $\gamma = 0.5$:

$$L_{ss} = \frac{0.5c_{ss}}{\delta(E)} = \frac{0.5c_{ss}}{m_\delta}\left(1 + \left(\frac{\delta E_{50}}{E}\right)^{k_\delta}\right). \quad \textbf{[S13]}$$

For a biphasic "concave-down" curve to exist there has to be a plateau at some value of E above zero. In other words,

$$\frac{dL_{ss}}{dE} = 0 \text{ when } E > 0.$$

However,

$$\frac{dL_{ss}}{dE} = -k_\delta \frac{0.5c_{ss}}{m_\delta} \delta {E_{50}}^{k_\delta} E^{-k_\delta - 1} = 0.$$

The only solution is $E = 0$ when $k_\delta < -1$. No solution exists when $k_\delta \geq -1$ ($k_\delta \neq 0$). Hence, no biphasic relationship between cell number and matrix stiffness is observed at the steady state in this case.

Network Analysis of Signaling Pathways. A physical interaction network consisting of drug targets ("nodes") in this study was constructed using Cytoscape, open-source software for network analysis (43). The physical interaction data were derived from multiple databases through the software, including BioGrid and MiMI. The results from previous tandem affinity purification and immunoprecipitation experiments with human cells were used for analysis. The results were filtered further based on previously reported confidence scores (>0.3 out of 1.0) for each interaction that were computed from the number of interactions and type of experiment, and the number of citations provided for each interaction. The total of 19 nodes and 41 interactions were used to construct the network. The interactions were then clustered on the basis of network topology or "interconnectedness" by using the clusterMaker2 plugin and the GLay Community Clustering algorithm, which identifies heavily connected subclusters via iterative removal of edges from the network. Three distinct clusters were identified and plotted in the interaction map. Arrows were assigned based on established knowledge on AKT and MAPK pathways. Interactions within the same cluster were colored black, and those in different clusters were colored gray.

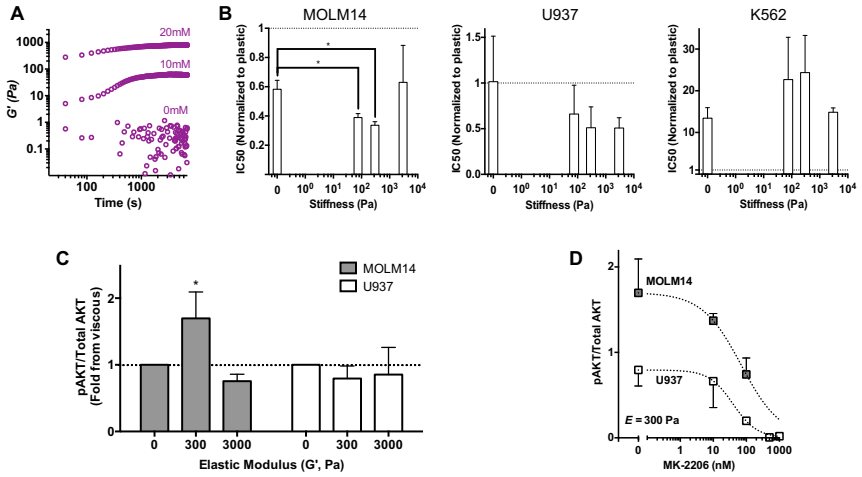

Fig. S1. (*A*) Mechanical characterization of alginate hydrogels formed by different calcium concentrations (millimolar) during gelation. G′ (pascals) is the shear storage modulus. (*B*) IC_{50} values for inhibition of cell proliferation across matrix stiffness by MK-2206. The IC_{50} values were normalized against corresponding values on plastic. Error bars indicate ± SEM, $n = 3$ experiments, $^*P < 0.05$ from one-way ANOVA with Tukey's HSD test (relative to 0 Pa). (*C*) Levels of pAKT in myeloid leukemia cells across matrix stiffness were evaluated by intracellular flow cytometry. $^*P < 0.01$ from one-way ANOVA with Tukey's HSD test (relative to 0 Pa). (*D*) Dose–response curves of pAKT inhibition by MK-2206 in leukemia cells encapsulated in 300-Pa gels. pAKT was measured by intracellular flow cytometry. Values normalized to pAKT of cells in untreated 0 Pa.

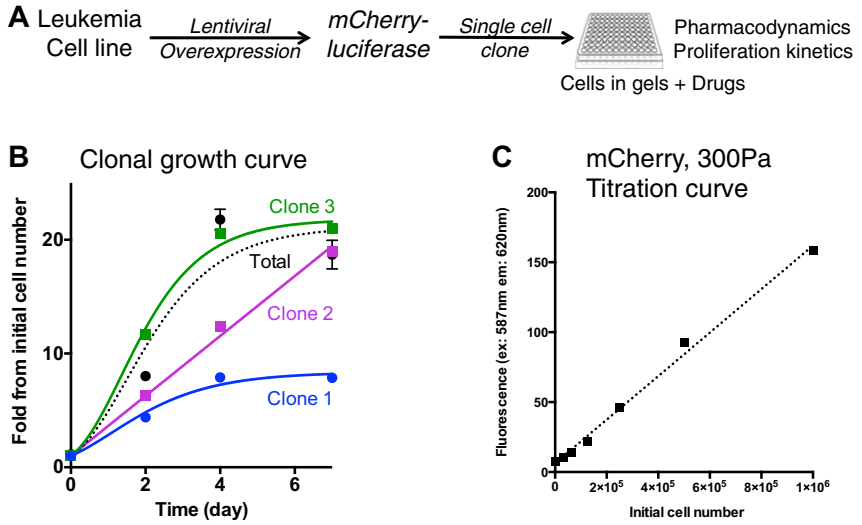

Fig. S2. Developing a screen to quantify proliferation and pharmacodynamics. (*A*) An overview of the screen approach. Cells were transduced with mCherry-luciferase by lentivirus followed by single-cell mCherry positive clone selection, expansion, encapsulation of cells in gels, and deposition in a 96-well. Cell proliferation kinetics in the presence of different drugs was then evaluated by fluorescence. (*B*) Cell proliferation kinetics of select mCherry-positive K-562 clones. (*C*) The graph showing mCherry fluorescence vs. cell number of clone 3 cells encapsulated in 300-Pa gels. Linear fit $R^2 > 0.95$.

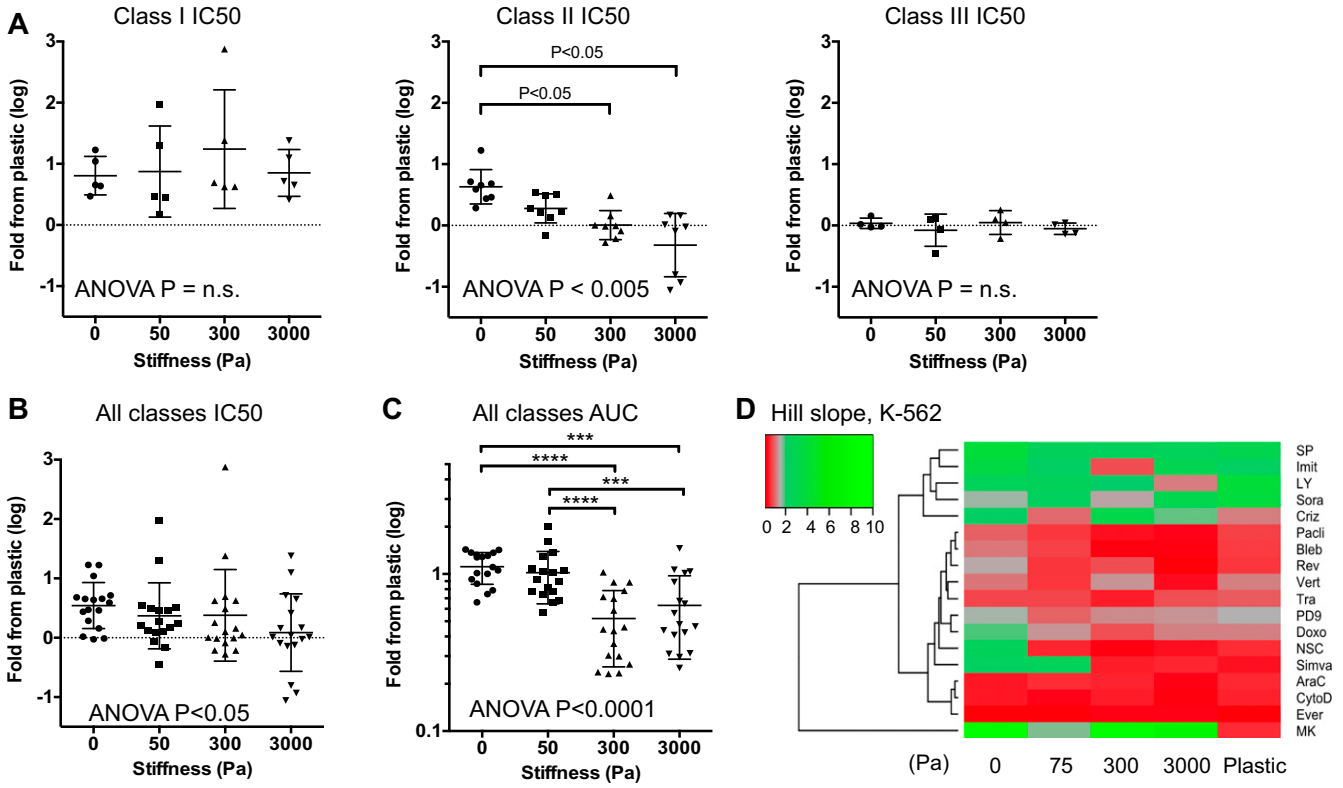

Fig. S3. (*A*) IC_{50} values of drugs from each drug class. For class II, one-way ANOVA $P < 0.005$, Tukey's HSD test $P < 0.05$, correlation analysis $P < 0.0001$. (*B*) IC_{50} values of drugs from all of the classes against K-562 cells across matrix mechanics. One-way ANOVA $P < 0.05$, followed by Tukey's HSD test. (*C*) AUC values of dose–response curves across matrix mechanics for K-562 cells. One-way ANOVA $P < 0.0001$, Tukey's HSD test ***$P < 0.005$, ****$P < 0.001$. In all graphs, values normalized to tissue culture plastic. (*D*) Clustering analysis of Hill slope values from individual drugs tested against K-562 cells.

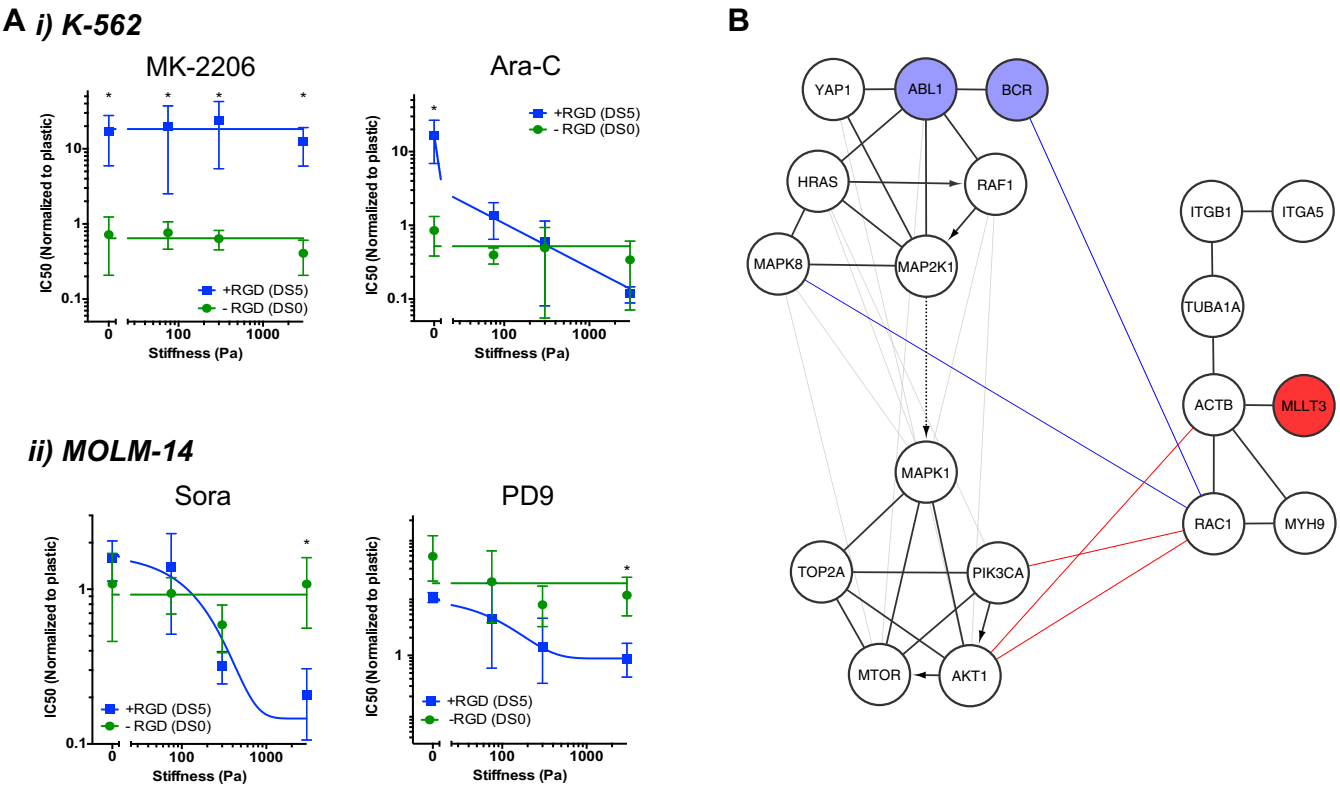

Fig. S4. (*A*) Drug resistance to class I and II drugs for K-562 (*i*) and MOLM-14 (*ii*) is integrin ligand-dependent. IC_{50} values derived from cells in hydrogels with (DS = 5) or without RGD were normalized against plastic and plotted across different mechanics. Error bars indicate ± SEM, $n = 3$ experiments, $^*P < 0.05$, paired *t* test. (*B*) Computational construction of a physical interaction network (*SI Methods*) reveals that proteins from protooncogenes of leukemias interact with distinct signaling clusters.

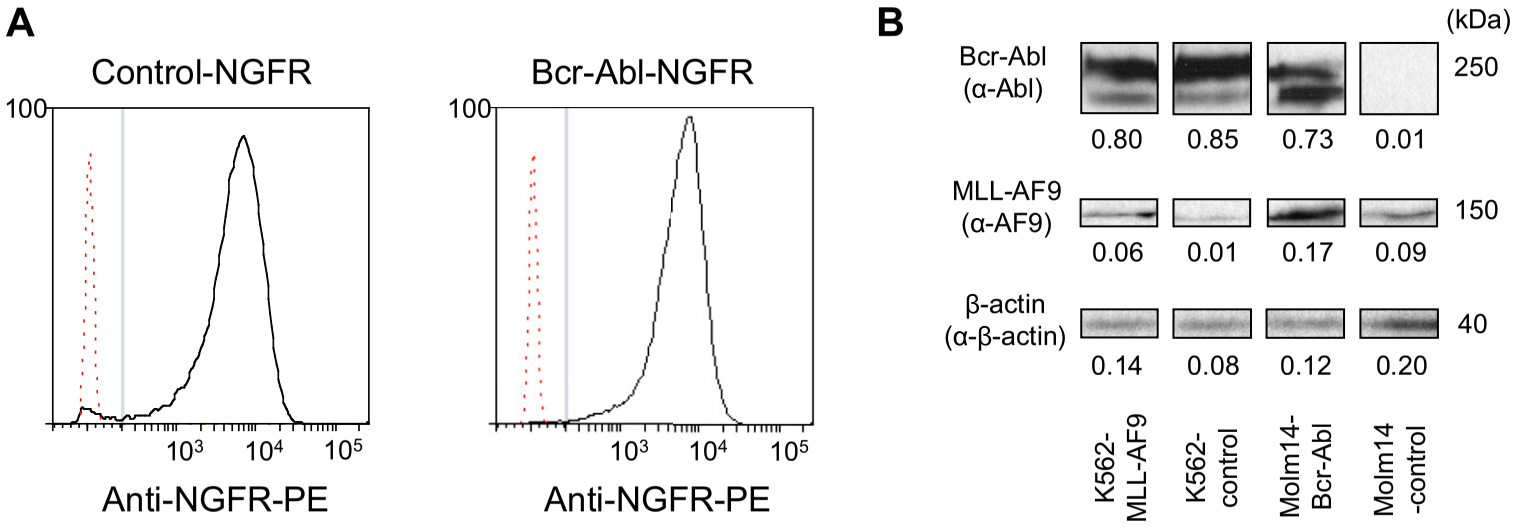

Fig. S5. (*A*) Transduction of MOLM-14 cells with a retroviral vector containing empty (*Left*) or Bcr-Abl (*Right*) confirmed by flow cytometry analysis. A truncated form of NGFR was used as a reporter to both sort transduced cells using FACS and confirm transduction efficiency using flow cytometry. A red dotted line in the flow cytometry plots indicates cells that are not transduced with a NGFR vector. (*B*) Protein expression of Bcr-Abl and MLL-AF9 in cells by Western blot.

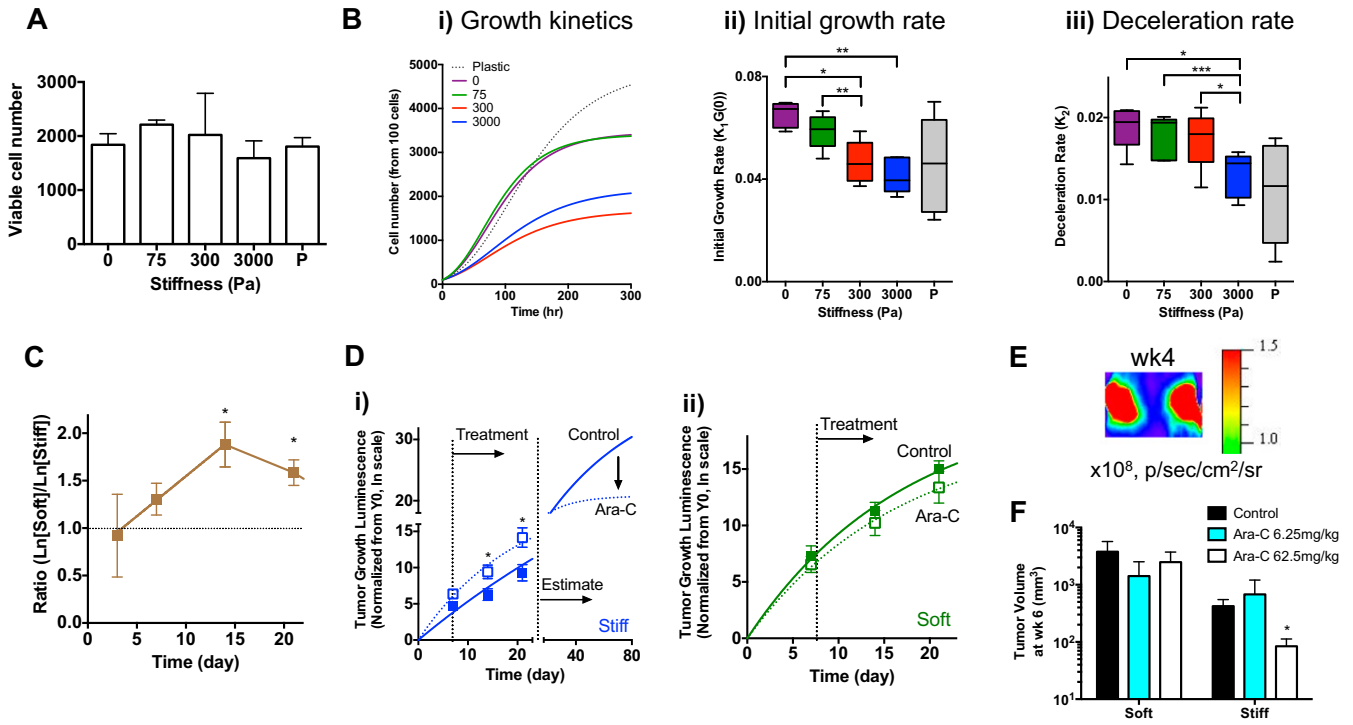

Fig. S6. (*A*) The number of viable cells after cell encapsulation in gels at day 0. (*B*) Slow but sustained growth of K-562 cells upon matrix stiffening. Matrix stiffness influences parameters of proliferation kinetics of K-562 cells. (*i*) Representative Gompertz curve fits (*SI Methods*) over 2 wk. (*ii*) Initial growth rate. (*iii*) Deceleration rate. For *ii* and *iii*, one-way ANOVA $P < 0.05$ with Tukey's HSD test, $*P < 0.05$, $**P < 0.01$, $***P < 0.005$. (*C*) K-562 cells in soft matrix show enhanced tumor growth compared with stiff matrix after s.c. implantation in vivo. Average radiance data from soft and stiff were converted to the natural log scale and divided (*SI Methods*). Straight line fit between day 3–14: $Y = 0.084t + 0.70$ (t: day). Data from $n = 15$ mice from three independent experiments. Paired *t* test, $*P < 0.005$. Error bars indicate ± SEM. (*D*) Tumor growth kinetics with Ara-C. (Plateau, acceleration rate) from the first-order kinetics fit for (*i*) stiff untreated (40, 0.56), Ara-C (20.8, 0.84) and (*ii*) soft untreated (22.5, 1.17), Ara-C (17.7, 1.15). Data from $n = 8$ mice from two independent experiments. Paired *t* test $*P < 0.05$. Error bars indicate ± SEM. (*E*) Bioluminescence signals become saturated at week 4. The same scale as in Fig. 4*A* was used. (*F*) Tumor volume at week 6 after implantation with different doses of Ara-C. Data from $n = 5$ mice for each group from two independent experiments. One-way ANOVA with Tukey's HSD test $*P < 0.05$ control vs. 62.5mg/kg Ara-C. Error bars indicate ± SEM.

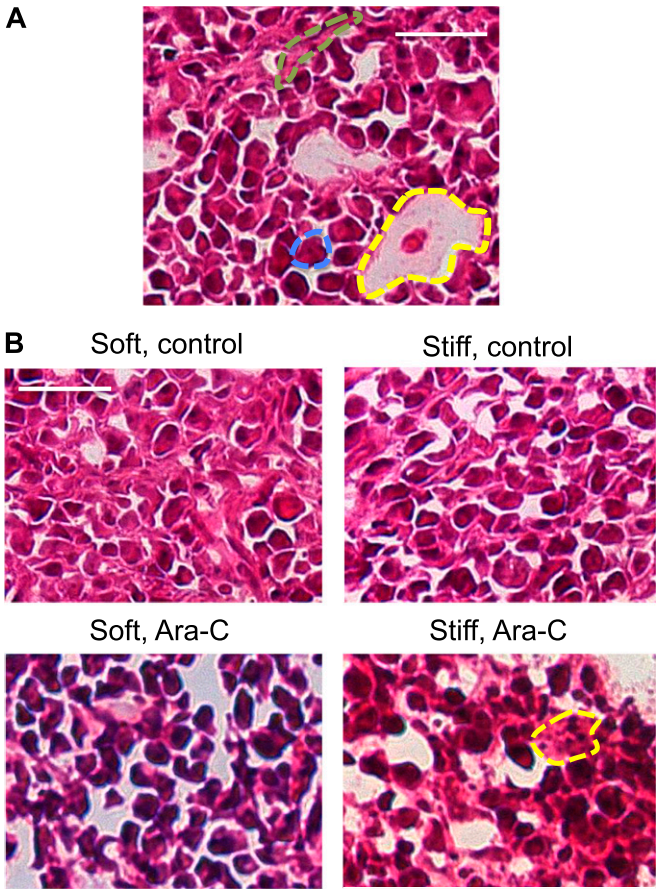

Fig. S7. Histological sections from s.c. implanted K-562 cells stained with hematoxylin and eosin. (*A*) A representative image showing blood cells (blue), stromal-like cells (green), and hydrogel fragments (yellow) after 2 wk of tumor implantation. (*B*) Representative images showing general morphological features of different treatment groups. Yellow: A region with nuclear fragments. (Scale bars: 50 μm.)

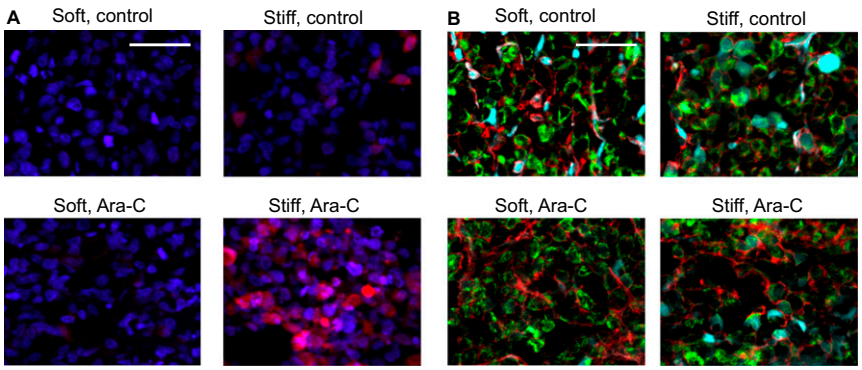

Fig. S8. Immunofluorescence staining of histological sections from s.c. implanted K-562 cells. (*A*) Representative images showing nuclei (blue) and cleaved caspase-3 (red). (Scale bar: 50 μm.) (*B*) Representative images showing F-actin (red), human mitochondria (green), and YAP (cyan). (Scale bars: 50 μm.)

Table S1. List of tested drugs and dose ranges

Drug	Abbreviation	Pathway	Tested dose range, nM
Everolimus	Ever	mTOR	0.1–1,000
MK-2206	MK	Akt	10–50,000
Doxorubucin	Doxo	DNA topoisomerase 2 (TOP2)	0.1–100
Crizotinib	Criz	c-MET kinase	0.1–1,000
Verteporfin	Vert	YAP/TAZ	10–2,000
Imitinib	Imit	ABL/KIT	0.1–100
Trametinib	Tra	MEK	0.1–100
NSC23766	NSC	Rac	100–50,000
Reversine	Rev	MEK, myosin-II	10–5,000
Paclitaxil	Pacli	Microtubule	10–1,000
Cytarabine	AraC	DNA synthesis	1–100
Blebbistatin	Bleb	Myosin-II	1,000–20,000
Simvastatin	Simva	Cholesterol	100–50,000
Sorafenib	Sora	RAF	100–5,000
SP600125	SP	JNK	5,000–40,000
PD98059	PD9	MAPK/ERK	10–50,000
Fasudil		Rho-kinase	300–20,000
Ruxolitinib		JAK	10–10,000